

The Different Dynamic Influences of Typhoon Kalmaegi on two Pre-existing Anticyclonic Ocean Eddies

Yihao He¹, Xiayan Lin^{1,2,*}, Guoqing Han¹, Yu Liu^{1,3} and Han Zhang^{2,3,*}

¹ Marine Science and Technology College, Zhejiang Ocean University, Zhoushan 316022, China;

² State Key Laboratory of Satellite Ocean Environment Dynamics, Second Institute of Oceanography, Ministry of Natural Resources, Hangzhou 310012, China;

³ Southern Marine Science and Engineering Guangdong Laboratory (Zhuhai), Zhuhai 519082, China

*Correspondence: Xiayan Lin (linxiayan@zjou.edu.cn) and Han Zhang (zhanghan@sio.org.cn)

Abstract: Using multi-source observational data and GLORYS12V1 reanalysis data, we conduct a comparative analysis of different responses of two warm eddies, AE1 and AE2 in the northern South China Sea to Typhoon Kalmaegi during September 2014. The findings of our research are as follows: (1) For horizontal distribution, the area and the sea surface temperature (SST) of AE1 and AE2 decrease by about 31% (36%) and 0.4 °C (0.6 °C). The amplitude, Rossby number (R_o =relative vorticity/Coriolis parameter) and eddy kinetic energy (EKE) of AE1 increases by 1.3 cm (5.7%), 1.4×10^{-2} (20.6%) and 107.2 $\text{cm}^2 \cdot \text{s}^{-2}$ (49.2%) after the typhoon, respectively, while AE2 weakens and the amplitude, Rossby number and EKE decreased by 3.1 cm (14.6%), 1.6×10^{-2} (26.2%) and 38.5 $\text{cm}^2 \cdot \text{s}^{-2}$ (20.2%), respectively.

(2) In vertical direction, AE1 demonstrates enhanced convergence, leading to an increase in temperature and a decrease in salinity above 150 m. The response below the mixing layer depth (MLD) is particularly prominent (1.3 °C). In contrast, AE2 experiences cooling and a decrease in salinity above the MLD. Below the MLD, it exhibits a subsurface temperature drop and salinity increase due to the upwelling of cold water induced by the suction effect of the typhoon. (3) The disparity in the responses of the two warm eddies can be attributed to their different positions relative to Typhoon Kalmaegi. Warm eddy AE1, with its center located on the left side of the typhoon's path, experiences a positive work effect as the typhoon passes by. The negative wind stress curl in AE1 triggers a negative Ekman pumping velocity (EPV), further enhanced by the converging sinking of the upper warm water, thereby strengthening AE1. On the other hand, warm eddy AE2, situated closer to the center of the typhoon, weakens due to the cold suction caused by the strong positive wind stress curl in the typhoon's center. Same polarity eddies may have different responses to typhoons, the distance between eddies and typhoons, eddies intensity and the background field need to be considered.

删除了: cm^2

删除了: cm^2

33 **1. Introduction**

34 Tropical cyclones (TCs), as they traverse the vast ocean, interact with oceanic mesoscale processes,
35 particularly with mesoscale eddies, representing a crucial aspect of air-sea interaction (Shay and Jaimes,
36 2010; Lu et al., 2016; Song et al., 2018; Ning et al., 2019; Sun et al., 2023). The South China Sea (SCS)
37 experiences an average of six TCs passing through each year (Wang et al., 2007), causing prominent
38 exchange of energy and mass between air and sea interface (Price, 1981). Meanwhile, due to the influence
39 of the Asian monsoon, intrusion of the Kuroshio Current, and complex topography, the Northern South
40 China Sea (NSCS) also encounters frequent eddy activities (Xiu et al., 2010; Chen et al., 2011). These
41 mesoscale oceanic eddies often play significant roles in mass and heat transportation and air-sea
42 interaction. This unique setting offers an exceptional opportunity to investigate the generation, evolution,
43 and termination of mesoscale eddies and their interaction with TCs.

44 On one hand, from a thermodynamic perspective, TCs derive their development and sustenance
45 energy from the ocean. Pre-existing mesoscale eddies play a crucial role in the feedback mechanism
46 between the ocean and TCs. Cyclonic eddies (cold eddies) enhance the sea surface cooling effect under
47 TCs conditions, resulting in TCs weakening, due to their thermodynamic structures and cold-water
48 entrainment processes that reduce the heat transfer from the sea surface to the TCs through air-sea
49 interaction (Ma et al., 2017; Yu et al., 2021). In contrast, anticyclonic eddies (warm eddies) suppress this
50 cooling effect, leading to TCs intensification (Shay et al., 2000; Walker et al., 2005; Lin et al., 2011;
51 Wang et al., 2018). Warm eddies have a thicker upper mixed layer, which stores more heat. When a TC
52 passes through a warm eddy, it increases sensible heat and water vapor in TC's center, which are closely
53 related to the TC's intensification (Wada and Usui, 2010; Huang et al., 2022). Furthermore, the
54 downwelling within warm eddies hinders the upwelling of cold water, reducing the apparent sea surface
55 cooling caused by the TCs. These processes weaken the oceanic negative feedback effect and help to
56 sustain or even strengthen TC's development. While from a dynamic perspective, TCs cause the
57 strengthening of cyclonic eddies, leading to positive potential vorticity anomalies, then accelerates the
58 currents and exacerbates global warming, ultimately further promotes TCs enhancement (Zhang et al,
59 2020).

60 On the other hand, TCs also have a notable impact on the intensity, size, and movement of mesoscale
61 eddies. In general, TCs strengthen cold eddies and can even lead to the formation of new cyclonic eddies

62 in certain situations (Sun et al., 2014), while TCs accelerate the dissipation of anticyclonic eddies (Zhang
63 et al., 2020). The strengthening effect of TCs on cold eddies is related to the positions between cold
64 eddies and TCs, the intensity of eddies, and TC-induced geostrophic response (Lu et al., 2016; Yu et al.,
65 2019; Lu et al., 2023). Cyclonic eddies on the left side of the typhoon track were more intensely affected
66 by the typhoon, and eddies with shorter lifespans or smaller radii are more susceptible to the influence
67 of TCs. The dynamic adjustment process of eddy and the upwelling induced by TC itself leads to changes
68 in the three-dimensional structure of the cyclonic eddies, including ellipse deformation and re-
69 axisymmetrization on the horizontal plane, resulting in eddy intensification. The presence of cold eddies
70 not only exacerbates the sea surface cooling in the post-typhoon cold eddy region but also accompanies
71 a decrease in sea level anomaly (SLA), deepening of the mixed layer, a strong cooling in the subsurface,
72 increased chlorophyll-a concentration within the eddy, and substantial increases in EKE and available
73 potential energy (Shang et al., 2015; Liu and Tang, 2018; Li et al., 2021; Ma et al., 2021).

74 Generally, typhoons lead to a reduction of warm eddies, while the sea surface cooling is not
75 significant, typically within 1°C. However, there is a noticeable cooling and increased salinity in the
76 subsurface layer, accompanied by an upward shift of the 20°C isotherm, a decrease in heat and kinetic
77 energy (Lin et al., 2005; Liu et al., 2017; Huang and Wang, 2022). Lu et al. (2020) propose that typhoons
78 primarily generate potential vorticity input through the geostrophic response. When a TC passes over an
79 eddy, there is a significant positive wind stress curl within the typhoon's maximum wind radius, which
80 induces upwelling in the mixed layer due to the divergence of the wind-driven flow field. This upward
81 flow compresses the thickness of the isopycnal layers below the mixed layer, resulting in a positive
82 potential vorticity anomaly. By analyzing the time series of ocean kinetic energy, available potential
83 energy (APE), vorticity budget, and potential vorticity (PV) budget, Rudzin and Chen (2022) find that
84 the positive vertical vorticity advection caused the TC to eliminate the warm eddy from bottom to top
85 after passing through. Under the interaction of the strong TC wind stress in the eye area of the TC and
86 the subsurface ocean current field, the early-onset of a near-inertial wake caused the disappearance of
87 the warm eddy. However, the projection of TC wind stress onto the eddy and the relative position of the
88 warm eddy to the TC can lead to different responses. According to the classical description of TC-
89 induced upwelling, strong upwelling occurs within twice the maximum wind radius of the TC center,
90 while weak subsidence exists in the vast area outside the upwelling region (Price, 1981; Jullien et al.,
91 2012). The warm eddy locates directly beneath the TC's path weakens due to the cold suction caused by

删除了: typhoon

删除了: typhoon

删除了: typhoon

删除了: typhoon

删除了: typhoon's

97 the TC's center. However, for warm eddies locate beyond twice the maximum wind radius, they are
98 influenced by the typhoon's wind stress curl and the downwelling within the eddy itself, resulting in the
99 convergence of warm water in the upper layers of the eddy, an increase in mixed layer thickness, and an
100 increase in heat content, leading to a warming response to the TC (Jaimes and Shay, 2015).

删除了: typhoon's

101 The NSCS encounters high frequency and intense TCs, concurrently, there is notable activity of
102 mesoscale eddies in this region. Based on in-situ datasets, multi-platform satellite measurements, and
103 GLORYS12V1 reanalysis data, we investigate two anticyclonic eddies on upper ocean responses to
104 Typhoon Kalmaegi. This marks the initial effort to characterize the different physical variations induced
105 by TCs within two same polarity eddies, contributing to a better understanding the role played by
106 mesoscale eddies in modulating interactions between TCs and the ocean. Section 2 provides an overview
107 of the data and methods utilized in this research. Section 3 analyzes the physical parameters of warm
108 eddies, vertical temperature and salinity variations, and explores the different responses of warm eddies
109 both inside and outside the typhoon affected region. Section 4 offers a comprehensive discussion and
110 Section 5 gives a summary.

删除了: typhoon

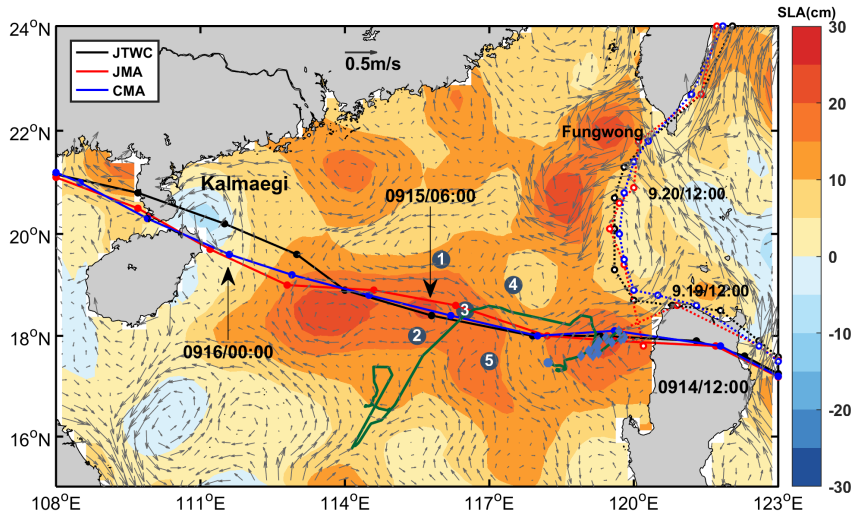
删除了: tropical cyclones (

删除了:)

111 2. Data and Methods

112 2.1. Data

113 The six-hourly best-track typhoon datasets are obtained from the Joint Typhoon Warning Center
114 (JTWC, <http://www.usno.navy.mil/JTWC>, last access: 3 February, 2021), the Japan Meteorological
115 Agency (JMA, <https://www.jma.go.jp/jma/jma-eng/jma-center/rsmc-hp-pub-eg/besttrack.html>, last
116 access: 3 February, 2021), and the China Meteorological Administration (CMA,
117 <http://tcdata.typhoon.gov.cn>, last access: 3 February, 2022). The data contain the TCs' center locations,
118 the minimum central pressure, maximum sustained wind speed, and intensity category. The translation
119 speed of typhoons is calculated by dividing the distance travelled by each typhoon within a 6-hour
120 interval by the corresponding time. In this paper, Typhoon Kalmaegi and tropical storm Fung-wong are
121 studied (Fig. 1).



126
 127 **Figure 1.** The tracks of Typhoon Kalmaegi (solid lines with dots) and tropical storm Fung-wong (dashed lines with
 128 hollow dots) as provide by the Joint Typhoon Warning Center (JTWC, black), Japan Meteorological Agency (JMA,
 129 red), and China Meteorological Administration (CMA, blue). The colour shading represents the sea surface level
 130 anomaly on 13 September, 2014, while the gray arrows illustrate the geostrophic flow field. The numbered blue dots
 131 represent the positions of the five buoy/mooring stations, the green line illustrates the trajectory of Argo 2901469,
 132 and the blue diamond's mark the positions of Argo 2901469 inside the eddy AE2 from 26 August 2014 to 25 October
 133 25, 2014.

134 The daily Sea Level Anomaly (SLA) and geostrophic current data provide by Archiving, Validation,
 135 and Interpretation of Satellite Data in Oceanography (AVISO) product (CEEMS,
 136 <https://marine.copernicus.eu/>, last access: 14 February, 2022). This dataset combines satellite data from
 137 Jason-3, Sentinel-3A, HY-2A, Saral/AltiKa, Cryosat-2, Jason-2, Jason-1, T/P, ENVISAT, GFO, and
 138 ERS1/2. The spatial resolution of the product is $1/4^\circ \times 1/4^\circ$, the period from 1 September to 30 September
 139 2014 was used.

140 The daily Sea Surface Temperature (SST) data used in this study is derived from the Advanced Very
 141 High-Resolution Radiometer (AVHRR) product data provided by the National Oceanic and Atmospheric
 142 Administration (NOAA). The data is obtained from the Physical Oceanography Distributed Active
 143 Archive Center (PODAAC) at the NASA Jet Propulsion Laboratory (JPL)
 144 (ftp://podaac.jpl.nasa.gov/documents/dataset_docs/avhrr_pathfinder_sst.html, last access: 16 March,
 145 2022). The spatial resolution of the data is $1/4^\circ \times 1/4^\circ$.

146 Argo data, including profiles of temperature and salinity from surface to 2000 m depth are obtained
 147 from the real-time quality-controlled Argo data base (Euro-Argo, <https://dataselection.euro-argo.eu/>, last
 148 access: 4 April, 2022). We select Argo float number 2901469, situated in an ocean anticyclonic eddy and
 149 in close proximity to Typhoon Kalmaegi, both before and after the typhoon's passage in 2014. Profiles
 150 of this Argo are also used to validate the vertical distribution of temperature and salinity from
 151 GLORYS12V1.

删除了: typhoon

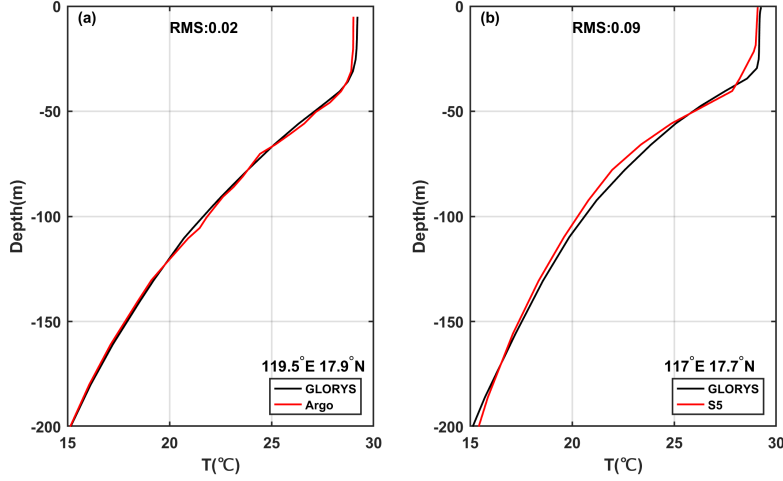
153 For this study, we also utilize in-situ data from a cross-shaped array consisting of five stations,
154 comprising five moored buoys and four subsurface moorings (refer to Fig. 1). More specific information
155 can be found in Zhang et al. (2016). To investigate the impact of the typhoon on a warm eddy, we select
156 the temperature and salinity data from Station 5, situated along the left track of Kalmaegi.

157 The wind speed data is sourced from the European Centre for Medium-Range Weather Forecasts
158 (ECMWF) ERA-Interim reanalysis assimilation dataset ([https://apps.ecmwf.int/datasets/data/interim-
159 full-daily/levtype=sfc/](https://apps.ecmwf.int/datasets/data/interim-full-daily/levtype=sfc/), last access: 5 January, 2023). This dataset is widely used for weather analysis
160 and numerical forecasting. The wind field data used in this study primarily focuses on the reanalysis data
161 of surface winds at a height of 10 meters above sea level for TCs. The selected data has a spatial
162 resolution of $1/4^\circ \times 1/4^\circ$ and a temporal resolution of 6 hours, with four updates per day (00:00, 06:00,
163 12:00, and 18:00 UTC). The data utilize corresponds to September 2014.

164 The Global Ocean Reanalysis Product GLOBAL_REANALYSIS_PHY_001_030 (GLORYS12),
165 provides by the Copernicus Marine Environment Monitoring Service (CMEMS,
166 <https://marine.copernicus.eu/>, last access: 23 March, 2022) is used in this study too. This reanalysis
167 product utilized the NEMO 3.1 numerical model coupled with the LIM2 sea ice model, and forced with
168 ERA-Interim atmospheric data. The model assimilated along-track altimeter data from satellite
169 observations (Pujol et al., 2016), satellite sea surface temperature data from AVHRR, sea ice
170 concentration from CERSAT (Ezraty et al., 2007), and vertical profiles of temperature and salinity from
171 the CORAv4.1 database (Cabanes et al., 2012). The temperature and salinity biases were corrected using
172 a 3D-VAR scheme. The horizontal resolution is $1/12^\circ \times 1/12^\circ$, and it has 50 vertical levels. The
173 temperature and salinity **form** 1 September to 30 September 2014 **were** chosen to study.

174 GLORYS12V1 is a widely used and applicable dataset, to evaluate its temperature profiles, the Argo
175 profiles and in-situ data of Station 5 were compared (Fig. 2). The GLORYS12V1 data exhibit good
176 agreement with Argo profiling floats, the maximum difference between them is less than 0.2°C , the Root
177 Mean Square (RMS) is 0.02. However, there are some discrepancies between the GLORYS12V1 and
178 the Station 5 data, with the largest difference occurring at the depths of 30 m (mixed layer) and 78 m
179 (thermocline), both differing by 0.6°C , while below 150 m, the difference is quite small. The RMS is
180 0.09. The RMS between GLORYS12V1 and Station 2 (Station 4) is 0.14 (0.10) (Figures not shown).
181 Because the GLORYS12V1 assimilates with Argo data and the vertical resolution of upper 100 m in
182 Argo profile is 5 m, but the vertical interval of buoy array is 20 m. Therefore, the large deviations exist
183 at mixed layer and thermocline during the typhoon in in-situ data of Station 5. Overall, GLORYS12V1
184 reproduces the observed ocean temperature accurately, it is reasonable to use it to investigate the vertical
185 response of anticyclonic eddies by [Typhoon](#) Kalmaegi.

删除了: typhoon



187
 188 **Figure 2.** Evaluation of GLORYS12V1 data performance during September 2014. (a) Vertical monthly mean
 189 temperature within the anticyclonic eddy AE2 (119.5°E 17.9°N) as measured by Argo float 2901469. (b)
 190 Comparison of vertical monthly mean temperature recorded at Station 5 (117°E 17.7°N).

191 **2.2. Methods**

192 Vorticity is a vector that characterizes the local rotation within a fluid flow. Mathematically, it is
 193 defined as the curl of the velocity vector. In most cases, when referring to vorticity, it specifically pertains
 194 to the vertical component of the vorticity. It is calculated from:

195
$$\zeta = \frac{\partial v}{\partial x} - \frac{\partial u}{\partial y} . \quad (1)$$

196 u and v are the zonal (eastward) and meridional (northward) geostrophic velocities, respectively. They
 197 are derived from altimeter sea level anomaly data (η):

198
$$u = -\frac{g}{f} \frac{\partial \eta}{\partial y} , v = \frac{g}{f} \frac{\partial \eta}{\partial x} . \quad (2)$$

199 Here, g is the acceleration of gravity, f is the Coriolis frequency. Vorticity is considered a
 200 fundamental characteristic of mesoscale eddies, positive vorticity signifies cyclonic eddies, while
 201 negative vorticity indicates anticyclonic eddies.

202 The Rossby number (Ro) is a dimensionless number describing fluid motion, and it is the ratio of
 203 relative vorticity to planetary vorticity, reflecting the relative importance of local non-geostrophic motion
 204 to large-scale geostrophic motion. The larger the Rossby number, the stronger the local non-geostrophic
 205 effect, and the definition of this parameter is:

206
$$Ro = \frac{\zeta}{f} . \quad (3)$$

207 Eddy Kinetic Energy (EKE) is a measure of the energy associated with mesoscale eddies, which
 208 indicates the intensity of eddies. It is typically calculated using the anomalies of the geostrophic velocity:

$$209 \quad EKE = \frac{1}{2}(u'^2 + v'^2) , \quad (4)$$

210 where u' represents the anomaly of the geostrophic zonal (eastward) velocity, v' represents the anomaly
 211 of the meridional (northward) velocity.

212 To evaluate the impact of a typhoon on an anticyclonic eddy, the calculation begins with determining
 213 the wind stress:

$$214 \quad \tau = \rho_a C_d U_{10} \overline{U_{10}} , \quad (5)$$

215 where ρ_a is the air density, assumed to be a constant value of 1.293 kg m^{-3} , U_{10} represents the 10-
 216 meter wind speed. And C_d is the drag coefficient at the sea surface (Oey et al., 2006):

$$217 \quad C_d \times 1000 = \begin{cases} 1.2 & U_{10} \leq 10 \text{ m s}^{-1} \\ 0.49 + 0.65 U_{10} & 11 \leq U_{10} < 19 \text{ m s}^{-1} \\ 1.364 + 0.234 U_{10} - 0.00023158 U_{10}^2 & 19 \leq U_{10} \leq 100 \text{ m s}^{-1} \end{cases} . \quad (6)$$

218 The wind stress curl is calculated by (Kessler, 2006):

$$219 \quad \text{curl}(\tau) = \frac{\partial \tau_y}{\partial x} - \frac{\partial \tau_x}{\partial y} , \quad (7)$$

220 where τ_x and τ_y are the eastward and northward wind stress vector components, respectively. The curl
 221 represents the rotation experienced by a vertical air column in response to spatial variations in the wind
 222 field.

223 The Ekman pumping velocity (EPV) represents the ocean upwelling rate, which can be used to study
 224 the contribution of typhoons to regional ocean upwelling. Positive means upwelling, negative represents
 225 downwelling:

$$226 \quad EPV = \text{curl}\left(\frac{\tau}{\rho f}\right) , \quad (8)$$

227 where the wind stress is obtained from Eq. (7), ρ is seawater density, the value is 1025 kg m^{-3} , and f
 228 is the Coriolis frequency.

229 The buoyancy frequency is a measure of the degree to which water is mixed and stratified. In a stable
 230 temperature stratification, the fluid particles move in the vertical direction after being disturbed, and the
 231 combined action of gravity and buoyancy always makes them return to the equilibrium position and
 232 oscillate due to inertia. When $N^2 < 0$, the water is in an unstable state:

$$233 \quad N^2 = -\frac{g}{\rho} \frac{\partial \rho}{\partial z} \quad (9)$$

234 where ρ is seawater density, g is the acceleration of gravity, and z is the depth.

235 **3. Results**

236 **3.1. Typhoon and pre-existing eddies in the NSCS**

237 **3.1.1. Track of Typhoon Kalmaegi and tropical storm Fung-wong**

238 Typhoon Kalmaegi strengthens into a typhoon by 1200 UTC on 13 September and emerged over the
239 warm waters of the Northern South China Sea (NSCS) by 1500 UTC on 14 September, with maximum
240 sustained winds of 33 m s^{-1} (Fig. 3-4). During this period, the NSCS experiences predominantly weak
241 vertical wind shear and is characterized by multiple anticyclonic warm eddies (Fig. 3). Subsequently,
242 Typhoon Kalmaegi undergoes two rapid intensification phases between 15 and 16 September. The first
243 intensification occurs at 0000 UTC on 15 September, propelling Kalmaegi to category 1 status with
244 surface winds surpassing 35 m s^{-1} . By 1200 UTC on 15 September, Kalmaegi experiences a second, even
245 more rapid intensification, with winds reaching 40 m s^{-1} in less than 12 hours. Throughout this
246 intensification stage, Kalmaegi encounters two warm eddies: anticyclonic eddy AE1, is positioned to the
247 left of the typhoon's path, with its core situates on the periphery of the typhoon's two-times maximum
248 wind radius (Fig.3c-d). AE1 has a lifespan of 105 days from 26 June to 8 October and is positioned at
249 17°N - 20°N , 113°E - 116°E . AE2 precisely intersecting with the typhoon's trajectory, and its core nearly
250 coincides with the maximum wind radius of the typhoon (Fig.3b-d). It has a lifespan of 89 days from 24
251 August to 20 November and is located at 17°N - 19°N , 118°E - 120°E . Kalmaegi makes landfall on Hainan
252 Island at 0300 UTC on 16 September, with a minimum central pressure of 960 hPa and a maximum wind
253 speed of 40 m s^{-1} . After landfall, Typhoon Kalmaegi gradually weakens and dissipates. During its
254 crossing of the NSCS, the five mooring stations are affected. Stations 1 and 4 are on the right side of
255 Typhoon Kalmaegi's track, while Stations 2 and 5 are on the left side. Unfortunately, the wire rope of the
256 buoy at Station 3 is destroyed by Kalmaegi, resulting in missing data from 15 September. Among the
257 stations, Station 5 is on the left of typhoon track and outside AE2, so its data is used in our study.

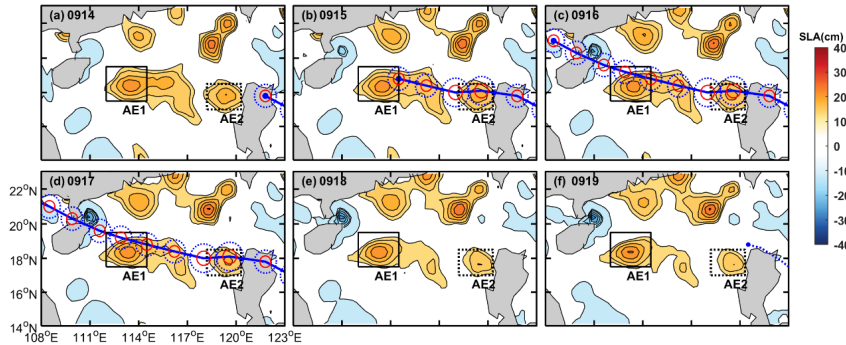
258 Tropical storm Fung-wong initially moves quickly in a northwest direction after formation. On 19
259 September, it enters the Luzon Strait and decelerates. It makes landfall in Taiwan on the 21 September
260 and subsequently lands in Zhejiang on the 22 September before gradually dissipating. When crossing the
261 Luzon Strait at 1200 UTC on 19 September, anticyclonic eddy AE2 is on the left side of Fung-wong,
262 with a distance of just over 100 km from its center.

删除了: m

删除了: m

删除了: Throughout this intensification stage, Kalmaegi encounters two warm eddies: anticyclonic eddy AE1, locates to the left of the typhoon's path, its core situates on the periphery of two times maximum wind radius of typhoon (Fig.3c-d)

删除了: AE2, precisely intersecting with the typhoon's trajectory, its core almost coincidents with maximum wind radius of typhoon (Fig.3b-d)...



272
273 **Figure 3.** The variations in sea level anomaly before and after Typhoon Kalmaegi moved over the anticyclonic eddies
274 AE1 and AE2 between 14 September and 19 September (a-f). The black solid rectangle represents the area of AE1,
275 while the black dashed rectangle represents the area of AE2. The blue solid line depicts the path of Typhoon
276 Kalmaegi, the solid red and dashed blue circles are the one- and two-times maximum wind radius of the typhoon,
277 while the blue dotted line in (f) is the path of tropical storm Fung-wong (best-track data sourced from CMA).

278 3.1.2. Eddy characteristics distribution

279 Satellite SLA measurements have proven to be highly effective and widely used for identifying and
280 quantifying the intensity of ocean eddies (Li et al., 2014). In Fig. 3, two warm eddies with clear positive
281 (> 13 cm) SLA are observed along the Typhoon Kalmaegi's track. During the period of 15 to 16
282 September, the typhoon passes over two warm anticyclonic eddies, AE1 and AE2. Before the typhoon,
283 AE1 is the most prominent eddy in the SCS, with an amplitude of 23.0 cm, and a radius of 115.5 km.
284 AE2, locates west of Luzon Island, exhibits an amplitude of 21.2 cm, with a radius of approximately
285 65.5 km. Tracing back to 2 months (figure is not shown), AE1 propagates slowly westward with about
286 $0.1 \text{ m}\cdot\text{s}^{-1}$, while AE2 is generated on 24 August. During 14 to 19 September, the amplitude of AE1
287 increases 1.3 cm. The area of the AE1 decreases by approximately 31% from $1.3 \times 10^5 \text{ km}^2$ to 9.1×10^4
288 km^2 and splits into two eddies. When Typhoon Kalmaegi crosses the core of AE2 at 1500 UTC on 14
289 September, and tropical storm Fung-wong moves over the northeast of AE2 at 1200 UTC on 19
290 September, the amplitude decreases by 3.1 cm. The area of the AE2 decreases by approximately 36%
291 from $4.2 \times 10^4 \text{ km}^2$ to $2.7 \times 10^4 \text{ km}^2$.

292 Because of intense solar radiation in September, the SST in the SCS is generally above 28.5°C prior
293 to the arrival of Typhoon Kalmaegi (Fig. 4a). As a fast-moving typhoon with a mean moving speed of
294 over $8 \text{ m}\cdot\text{s}^{-1}$, Kalmaegi induces a larger cooling area and intensity on the right side of its path compared
295 to the left side (Price, 1981). During the passage of Kalmaegi, the lowest SST on the right side of typhoon
296 decreases to 27.2°C . Even after the typhoon has passed, a cold wake could still be observed on the right
297 side of its path, persisting for over a week (Fig. 4c).

298 Mesoscale eddies, due to their special thermodynamic structure and varying positions in relation to
299 the TC, can modulate distinct sea surface temperature changes and exhibit different characteristics. The
300 pre-existing warm eddy AE1 begins to cool down before Kalmaegi reached the NSCS, dropping to

删除了: typhoon

删除了: typhoon

删除了: m

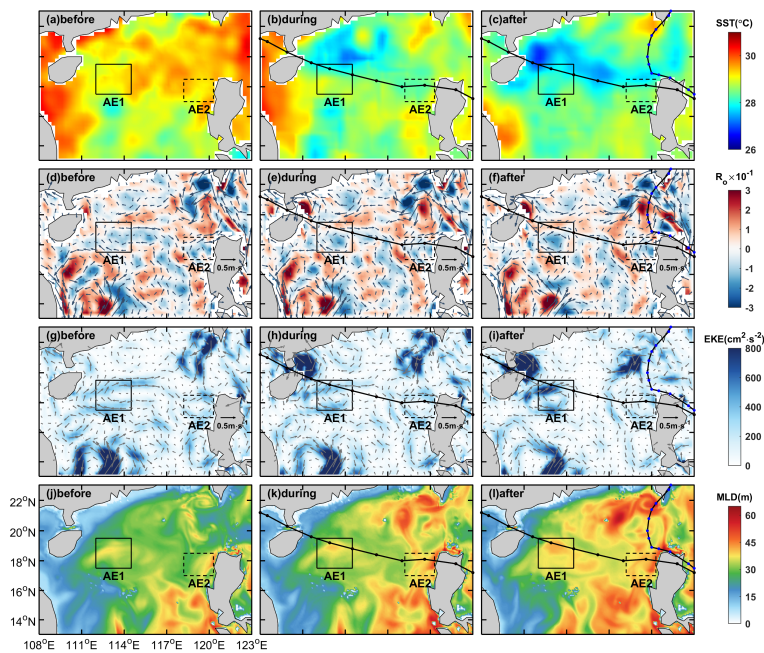
304 28.4°C on 14 September. During this period, the mean SST within AE1 increases slightly to 28.6 °C (Fig.
305 5a). However, as cooler water from the right side of the typhoon track is subsequently advected into the
306 AE1 region (Fig. 4c), the SST decreases and reaches 28.0 °C on September 19, which is 0.4°C lower
307 than that before the typhoon. The average SST drop in AE2 is relatively evident, with SST starting to
308 decline before 14 September and reaching its lowest temperature (28.1°C) on 15 September, 0.6 °C lower
309 than that before the typhoon (Fig. 5e). On 16 September, the SST within AE2 begins to recover, but it
310 starts to cool again on 18 September due to the influence of Fung-wong.

311 Then we compare the Ro and EKE of AE1 and AE2 before, during and after typhoon. Before being
312 influenced by the typhoon, the warm eddy AE1 exhibits a more scattered distribution of negative Ro due
313 to its edge structure, and the EKE values at the eddy boundary are relatively high (Fig. 4d, g). As the
314 typhoon passes through the eddy, the Ro and EKE of AE1 starts to increase. On 19 September, the
315 average Ro within AE1 reaches a value of -8.2×10^{-2} , at the same time, the average EKE increases to its
316 maximum value of $325.0 \text{ cm}^2 \cdot \text{s}^{-2}$. The variation trend of Ro and EKE within the eddy is consistent,
317 increasing from the passage of the typhoon and starting to recover on 20 September (Fig. 5b-c). This
318 indicates that although the area of the warm eddy AE1 decreased under the influence of the typhoon, its
319 intensity increases. On the other hand, for warm eddy AE2, both Ro and EKE decreases after the typhoon
320 passage, with the Ro decreasing to -4.5×10^{-2} on 17 September and the EKE decreasing to $152.0 \text{ cm}^2 \cdot \text{s}^{-2}$
321 on the 19 September, followed by a recovery (Fig. 5f-g). Unlike AE1, AE2 weakens in intensity under
322 the influence of the typhoon.

323 During the passage of the typhoon, enhances mixing driven by wind stress and increases vertical
324 shear result in a deepening of the MLD, which further strengthens the mixing between the deep cold
325 water and the upper warm water (Shay and Jaimes, 2009). To avoid a large part of the strong diurnal
326 cycle in the top few meters of the ocean, 10 m is set as the reference depth (De Boyer Montégut, 2004).
327 A 0.5 °C threshold difference from 10 m depth is calculated and defines as the MLD (Thompson and
328 Tkalic, 2014). Prior to the influence of typhoon Kalmaegi, the MLD in the AE1 and AE2 regions is
329 deeper (Fig. 4j), with the average MLDs of 32 m and 33 m, respectively. Starting from 14 September,
330 the MLDs are influenced by typhoon Kalmaegi, with the MLD of AE1 deepening to 37 m and that of
331 AE2 increasing to 41 m, representing a deepening of 5 m and 8 m, respectively (Fig. 5d, h).

332 Overall, Typhoon Kalmaegi likely exerts distinct impacts on the two warm eddies. Despite both AE1
333 and AE2 experiencing a decrease in their respective areas by approximately one-third, accompanies by
334 deepening of the MLD, the amplitude of SLA within AE1 increases by 1.3 cm, whereas AE2 witnesses
335 a decrease of about 3.1 cm in its amplitude. Furthermore, the SST, Rossby number and EKE within AE1
336 and AE2 exhibits contrasting patterns.

删除了: cm^2



338

339

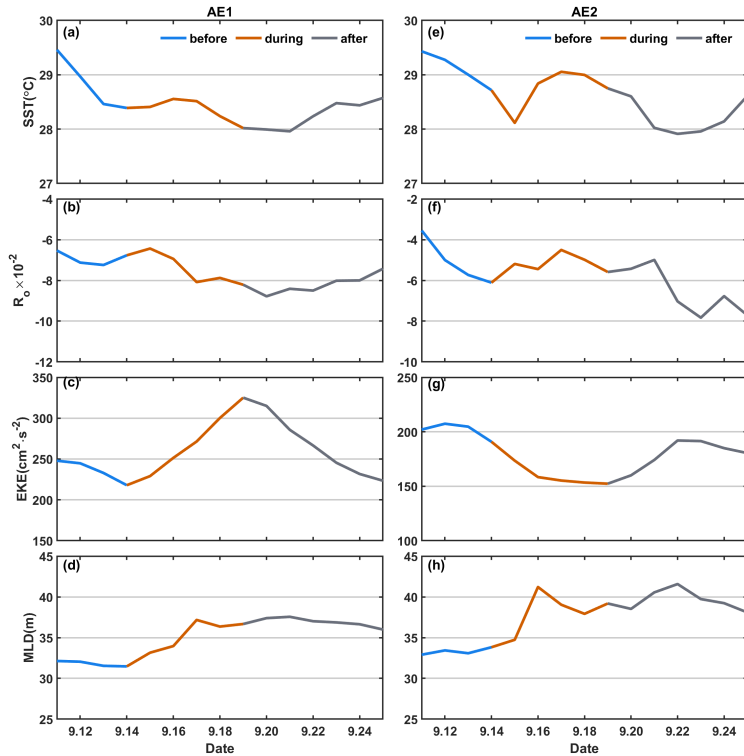
340

341

342

343

Figure 4. The spatial distribution of SST, R_e , EKE, and MLD before, during and after the passage of TCs. The time periods of 10-13, 15-16 and 19-22 September are designated as stages before, during and after Kalmaegi, respectively. The path of Typhoon Kalmaegi is depicted by a black solid line with black dots, while the path of tropical storm Fung-wong is represented by a black solid line with blue dots in the third column. The solid and dashed boxes correspond to AE1 and AE2, respectively.



344
 345 **Figure 5.** The time series of sea surface temperature (SST), R_σ , eddy kinetic energy, and mixed layer depth (MLD)
 346 within the warm eddies' regions (black solid and dashed boxes in Fig. 4). The first column is variables of AE1, the
 347 second column is for AE2.

348 3.2 Upper-ocean vertical thermal and salinity structure of eddies

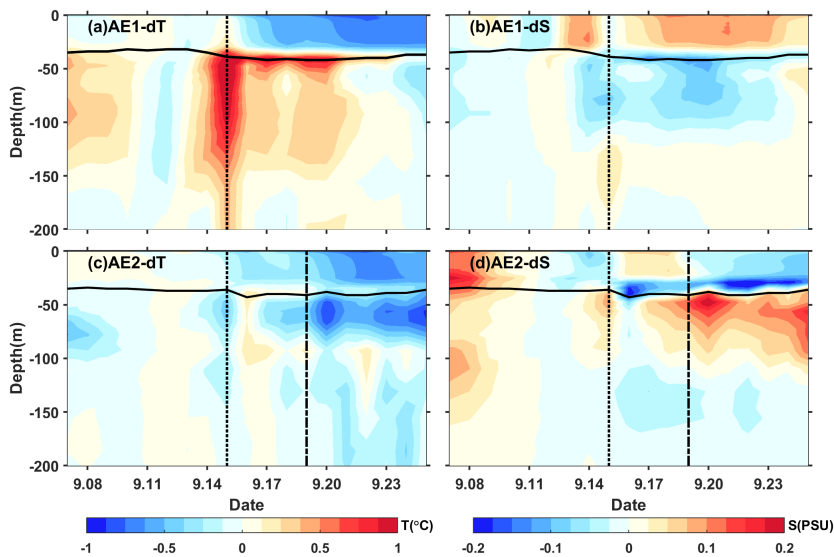
349 We conduct further analysis on the vertical temperature and salinity structure of the warm eddies
 350 AE1 and AE2 before and after the Typhoon Kalmaegi using GLORYS12V1 data. **During the typhoon's**
 351 **passage on 15 September**, the temperature above the MLD within AE1 increases by approximately 0.1 °C,
 352 while the salinity decreases by 0.02psu (Fig. 6). Below the MLD, the temperature shows a significant
 353 increase, reaching a maximum temperature rise of 1.3 °C. Correspondingly, the salinity below the MLD
 354 exhibits a decrease of 0.05 psu. Vertical temperature on Kalmaegi's arrival day **shows** warm pattern from
 355 surface to 200 m, the salinity **shows** "fresher-saltier" pattern. These changes lead to a deepening of the
 356 isodensity by 15 m and a decrease in buoyancy frequency N^2 (Fig. 7a-b), indicating convergence and
 357 downwelling within the centre of the warm eddy AE1. **The near-inertial waves propagate downward**
 358 **from surface to 200m from this period (Zhang et al, 2017). The transfer of energy from anticyclonic eddy**
 359 **to near-inertial waves is the main reason for the downward propagation and longtime persistence of near-**
 360 **inertial energy (Chen et al, 2023).**

361 After 15 September, the temperature above the MLD decreases, and the salinity shows an increase
 362 (Fig. 6a-b), resulting in the uplift of the 1021 $\text{kg}\cdot\text{m}^{-3}$ isodensity to the sea surface (Fig. 7a-b). The
 363 subsurface warming and salinity reduction gradually weakens after the Typhoon Kalmaegi but persists
 364 for about a week after the typhoon's passage until 22 September. During this period, vertical temperature
 365 pattern becomes "cool-warm" at the center of AE1, and the salinity distribution pattern becomes "saltier-
 366 fresher-saltier". This persistence can be attributed to the intensified stratification around the MLD, with
 367 N^2 around $9.0\times 10^{-4}\text{s}^{-2}$ (Fig. 7b). The increased stability inhibits vertical mixing, restrains the exchange
 368 of heat and salinity, and leads to smoother density gradients above the MLD (Fig. 7a).

369 The vertical temperature and salinity structure of AE2 exhibits an opposite trend. During the typhoon
 370 passage on 15 September, AE2 also experiences a cooling trend of $0.2\text{ }^\circ\text{C}$, with a decrease in salinity of
 371 0.04 psu above the MLD. Below the MLD, the temperature shows a consistent decrease, with a change
 372 of less than $0.5\text{ }^\circ\text{C}$ within the subsurface. Correspondingly, the salinity exhibits an increase of
 373 approximately 0.08 psu (Fig. 6c-d). The slightly upward shift of the isodensity (Fig. 7c) suggests the
 374 possibility of cold-water upwelling induced by the suction effect of the typhoon. The temperature
 375 decreases and salinity increases below the MLD are primarily driven by upwelling processes.

376 Furthermore, when the tropical storm Fung-wong passes through AE2 on 19 September (dashed line
 377 in Fig. 6c-d), the decreasing trend of subsurface temperature becomes more pronounced, and the
 378 subsurface salinity exhibits a significant increase. AE2 is more significantly influenced by tropical storm
 379 Fung-wong. It presents stable stratification with N^2 around $8.4\times 10^{-4}\text{s}^{-2}$ at a depth of 42 m , creating a
 380 barrier layer that prevents the intrusion of high-salinity cold water from the lower layers into the mixed
 381 layer (Yan et al., 2017).

382

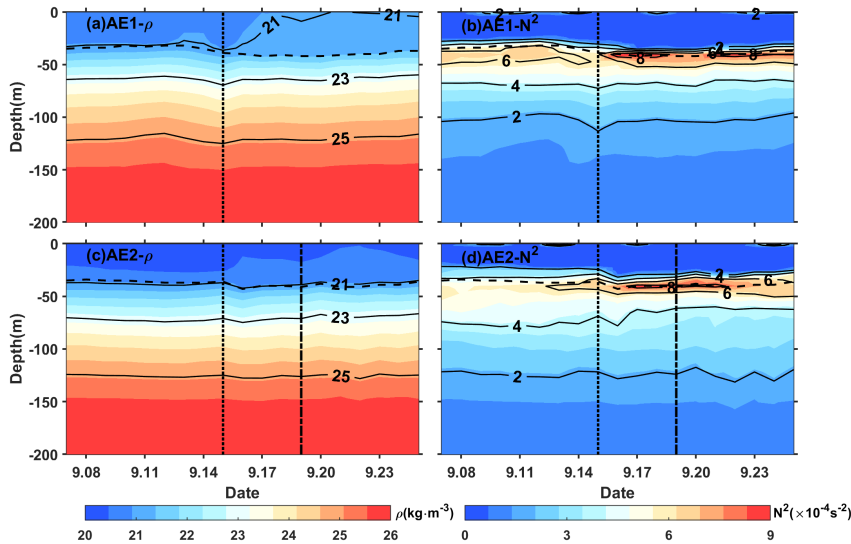


383

删除了: kg

385 **Figure 6.** The timeseries of vertical temperature and salinity anomalies in the center of AE1(a,b) and AE2 (c,d).
 386 The anomalies were calculated relative to the average value of 10-13 September. The vertical black dotted line
 387 indicates the Typhoon Kalmaegi's passage, while the vertical black dashed line represents the passage of tropical
 388 storm Fung-wong. The black solid line is the MLD.

删除了: t



389
 390 **Figure 7.** Same as Fig. 7, but for density and buoyancy frequency (N^2).

391 3.3 Comparison of the response between eddies and non-eddies areas

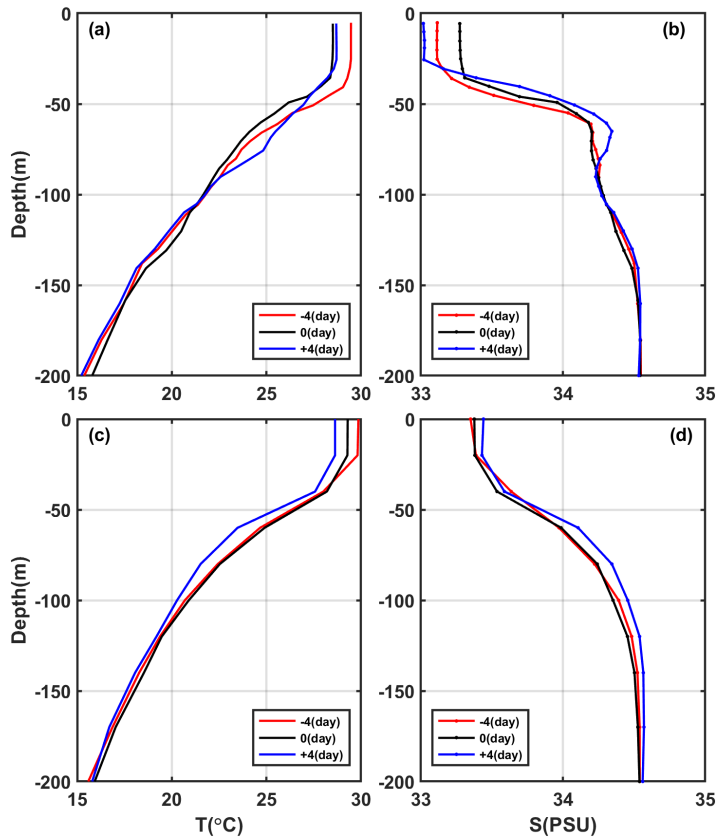
392 To investigate the contrasting response of warm eddies and the non-eddies background to Typhoon
 393 Kalmaegi, we conduct a comparative analysis of vertical temperature and salinity profiles in these two
 394 areas. Unfortunately, there is no Argo data around AE1, therefore, we examine data from Argo 2901469,
 395 which is located within AE2 during the period from 11 to 19 September. The temperature and salinity
 396 data from Station S5 is considered as the background, with S5 locates at a distance of 246 km from AE2's
 397 center on 15 September (Fig. 1). These profiles are categorized into three periods: pre-typhoon (11
 398 September), during-typhoon (15 September), and post-typhoon (19 September).

删除了: typhoon

399 At depths above 40m, both inside and outside of AE2 experiences a decrease in temperature, with a
 400 cooling of less than -1.0°C . Four days after the typhoon passage (19 September), the cooling persists
 401 inside and outside the eddy, with the cooling being more pronounced outside AE2, showing a decrease
 402 of 1.2°C (Fig. 8c). The salinity within AE2 initially increases by 0.15 psu from the pre-typhoon stage to
 403 the during-typhoon stage and then decreases by 0.09 psu after the typhoon passage (Fig. 8d). While the
 404 salinity at Station 5 shows a similar pattern in pre-typhoon and during-typhoon stage, it increases by 0.05
 405 psu after the typhoon. Two possible processes can explain the difference in salinity trends inside and
 406 outside AE2. First, during the pre-typhoon to typhoon stage, the entrainment within AE2 may have
 407 brought the subsurface water, which is saltier, up to the surface, resulting in an increase in salinity. The

410 second process is related to the typhoon-induced precipitation after the typhoon passage, which lead to a
411 decrease in salinity. Strong stratification have contributed to the persistence of saltier subsurface water.
412 While at S5, the increase in salinity is relatively minor only increased slightly.

413 On 15 September, the subsurface layer at 45 m to 100 m is affected by the cold upwelling, which is
414 caused by the typhoon, resulting in a cooling and increased salinity within AE2. As the forcing of
415 Typhoon Kalmaegi diminishes, the upper layer of seawater begins to mix, and influences by the
416 downward flow of the eddy itself, warm surface water is transported to the subsurface layer. Four days
417 later, a warming phenomenon occurs, with the maximum warm anomaly of 1.2 °C observes at a depth of
418 75 m (Fig. 8a). The mixing effect outside the eddy is not significant, resulting in a slight subsurface
419 warming of approximately 0.2 °C, with no significant changes in salinity. However, on 19 September, a
420 maximum cold anomaly of -1.2°C is observed at a depth of 60 m, corresponding to the maximum salinity
421 anomaly of 0.13 psu (Fig. 8c-d). Below 100 m, AE2 experiences a temperature increase of 0.5 °C and a
422 slight decrease in salinity of 0.04 psu. On 19 September, the temperature and salinity within AE2 shows
423 little change. However, outside the eddy, a different response is observed. On 19 September, a cooling
424 trend is observed throughout the water column, within a range of 0.2 °C, accompanies by a noticeable
425 increase in salinity (Fig. 8c, d), within a range of 0.06 psu. This indicates that the typhoon causes a
426 significant upwelling outside the eddy region.



427
 428 **Figure 8.** (a-b) the vertical profile of temperature and salt inside the eddy (Argo 2901469), (c-d) the vertical profiles
 429 of temperature and salt outside the eddy (S5). The red, black and blue lines represent pre-typhoon, during-typhoon
 430 and post-typhoon stages.

431 Based on Argo profiles and S5 data, the upper ocean above 200 m inside and outside AE2 responds
 432 differently to the forcing of the typhoon. In the upper layer (0-40 m), cooling is observed both inside and
 433 outside the eddy, and it lasts for a longer duration. In the subsurface layer (45-100m), after the passage
 434 of the typhoon (19 September), there is a strong cooling outside the eddy, while warming occurs within
 435 AE2. Zhang (2022) points out that the sea temperature anomalies mainly depend on the combined effects
 436 of mixing and vertical advection (cold suction). Mixing causes surface cooling and subsurface warming,
 437 while upwelling (downwelling) leads to cooling (warming) of the entire upper ocean. The temperature
 438 anomaly in the subsurface layer depends on the relative strength of mixing and vertical advection, with
 439 cold anomalies dominating when upwelling is strong, and downwelling amplifying the warming
 440 anomalies caused by mixing. Therefore, due to the strong influence of upwelling outside the eddy, the
 441 temperature profile of the entire water column shifts upwards, resulting in cooling of the entire upper
 442 ocean. On the other hand, influences by the downwelling associates with the warm eddy itself, a warming

443 anomaly of 1.2 °C is observed in the subsurface layer. Compares to region AE2, the cold suction effect
444 causes by the Typhoon Kalmaegi is still evident in the non-eddy area.

445 In the following sections, we delve into the underlying reasons behind these different responses of
446 AE1 and AE2 to Typhoon Kalmaegi.

447

448 4. Discussion

449 The EPV is very small before the typhoon, measuring less than $0.5 \times 10^{-5} \text{ m.s}^{-1}$ in both AE1 and AE2.
450 However, during 15-16 September (Fig. 9c-f), when typhoon crosses the NSCS, the EPV undergoes
451 significant changes. Its absolute value increases to over $1.5 \times 10^{-4} \text{ m.s}^{-1}$ within both AE1 and AE2. AE1
452 consistently exhibits a predominantly negative EPV during most of this period. Consequently, during
453 Typhoon Kalmaegi, the negative EPV facilitates downwelling and convergence (Jaimes and Shay, 2015),
454 leading to a warmer and fresher subsurface layer in AE1 (Fig. 6 a-b).

455 On the other hand, AE2 displays a more fluctuating pattern. It is positive on 14 September, shows
456 both positive and negative values at 0000 UTC on 15 September, and remains mainly negative from 15
457 to 16 September, and eventually returning to positive, reflecting a continuously fluctuating process. The
458 positive EPV in AE2 contributes to the influx of colder subsurface water into the upper layers, resulting
459 in surface and subsurface water cooling and an increase in salinity in the subsurface (Fig. 6c-d).
460 Correspondingly, the variations in Ekman layer depth (D_E) with the typhoon's passage are similar to EPV,
461 as shown in Fig. 10. When Kalmaegi approaches at 0000 UTC on 14 September, the mean D_E within
462 AE1 is only 21 m, while in AE2, it is 114 m. This indicates that AE2 has already been influenced by
463 Typhoon Kalmaegi. Subsequently, the depth of the DE within AE2 sharply deepens, reaching its
464 maximum depth of 241 m at 0000 UTC on 15 September, coinciding with the proximity of Typhoon
465 Kalmaegi's center to AE2. As Kalmaegi moves northwest, the D_E within AE1 achieves its maximum
466 depth of 262 m at 0000 UTC on 16 September. The trends of D_E within AE1 and AE2 are nearly
467 consistent, but AE1 lags behind AE2 by one day. Starting from 15 September, D_E within both AE1 and
468 AE2 gradually shallows, reaching a minimum D_E of 60 m. This value is 28 m higher than before the
469 typhoon, indicating the lingering effects of the typhoon through wind. For AE2, D_E reached its minimum
470 of 45 m at 0000 UTC on 18 September, later gradually increasing under the influence of tropical storm
471 Fung-wong.

设置了格式: 上标

删除了: The EPV of

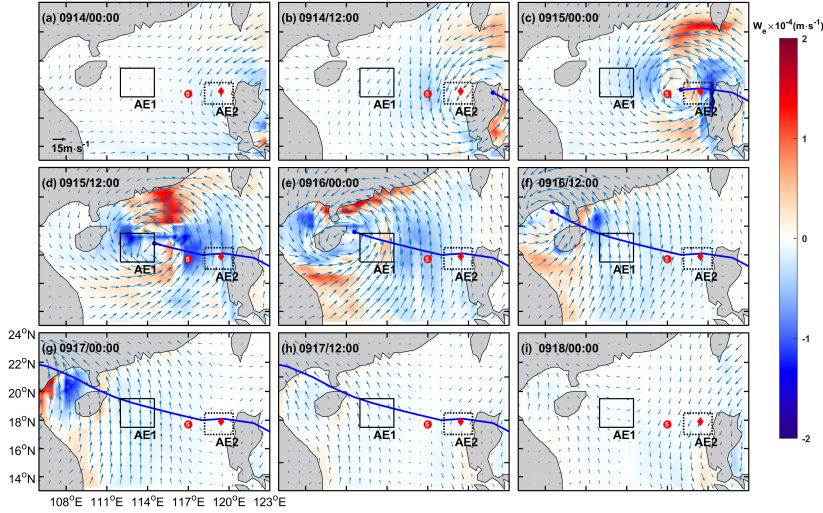
设置了格式: 上标

删除了: is

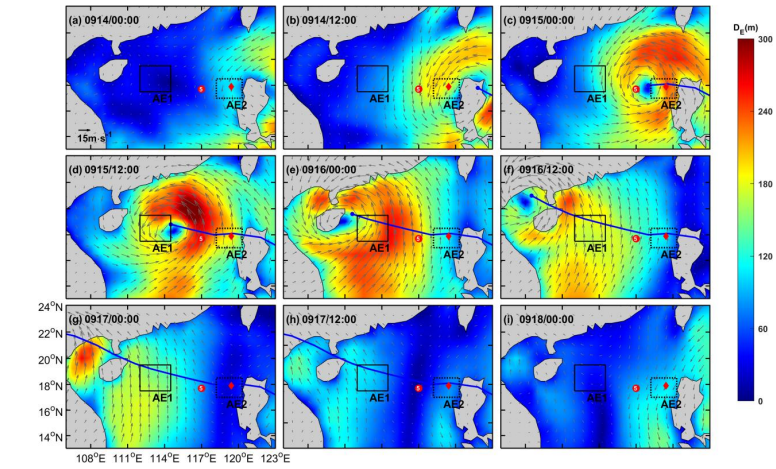
删除了: the time

删除了: typhoon

删除了: On the other hand, AE2 exhibits a more fluctuating pattern. It is positive on 14 September, has both positive and negative values at 0000 UTC on 15 September, and is mainly negative from 15 September to 16 September, and then becomes positive again, which is a constantly fluctuating process. The positive EPV in AE2 contributes to the influx of colder subsurface water into the upper layers, resulting in surface and subsurface water cooling and increases salinity in the subsurface (Fig. 6c-d). Correspondingly, the variations in Ekman layer depth (D_E) with the typhoon's passage are similar to EPV, as shown in Fig. 10. When Kalmaegi approaches at 0000 UTC on 14 September, the mean D_E within AE1 is only 21 m, while in AE2, it is 114 m. This indicates that AE2 has already been influenced by typhoon Kalmaegi. Subsequently, the depth of the DE within AE2 sharply deepens, reaching its maximum depth of 241 m at 0000 UTC on 15 September, coinciding with the proximity of typhoon Kalmaegi's center to AE2



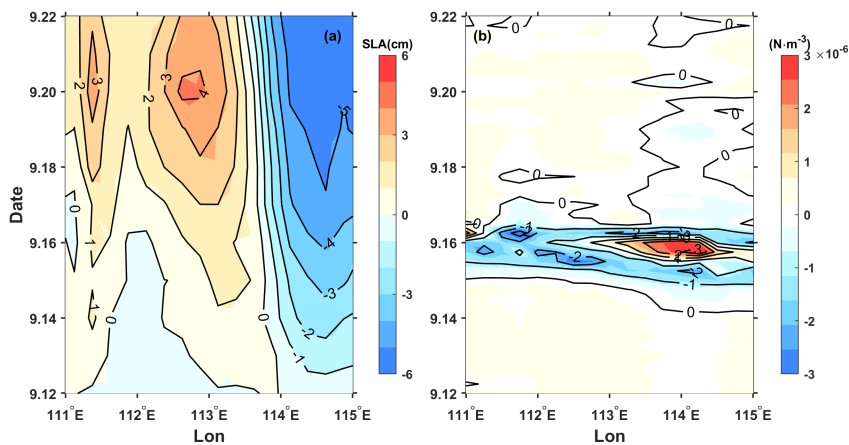
492
 493 **Figure 9.** Ekman Pumping Velocity (EPV) from 14 September to 18 September (a-i). The color represents the EPV,
 494 the blue solid line is the path of Kalmaegi, the red dot and diamond are the positions of Station 5 and Argo 2901469
 495 on 15 September, respectively.



496
 497 **Figure 10.** Ekman layer depth (D_E) from 14 September to 18 September (a-i). The color represents the D_E , the blue
 498 solid line is the path of Kalmaegi, the red dot and diamond are the positions of Station 5 and Argo 2901469 on 15
 499 September, respectively.

500 After traversing the warm ocean characteristics of AE2, Typhoon Kalmaegi strengthens, resulting in
 501 a reduction of the maximum wind radius. As it passed through AE1, the maximum wind radius is 35 km.
 502 Notably, the center of AE1 is located outside the typhoon's two-times maximum wind radius,
 503 approximately 104 km away from the typhoon center (Fig. 3). As mentioned earlier, strong upwelling
 504 occurs within two-times maximum wind radius, while weak subsidence exists in the vast area outside

505 the upwelling region (Jaimes and Shay, 2015). Hence, the hypothesis presents here suggests that the
 506 observed intensification of AE1 on the left side of the typhoon track is more likely attributed to the
 507 negative wind stress generates outside the maximum wind radius, driving the enhancement of
 508 downwelling in the pre-existing anticyclonic feature in the ocean. Starting from 15 September, a
 509 significant positive sea level anomaly (SLA) to the west of 113.5°E becomes evident, intensifying and
 510 reaching its maximum on 20 September (Fig. 11a). This strengthening aligns with the increase in the
 511 amplitude of the warm core of the eddy AE1. A comparison with the wind stress curl anomaly (Fig. 11b)
 512 reveals that between 15 to 16 September, as the Typhoon Kalmaegi moves over the section at 18.2°N,
 513 specifically to the west of 113.5°E, it exhibits strong negative wind stress curl anomalies, with a
 514 maximum intensity of $-3 \times 10^{-6} \text{ N.m}^{-3}$. The negative wind stress curl induces by the typhoon results in
 515 favourable surface ocean currents that further enhances the clockwise rotation of the warm eddy. The
 516 negative wind stress curl anomaly results strong downwelling currents, inputting negative vorticity into
 517 AE1, leading to its intensification (Fig. 4b-c), as indicates by the enhanced positive SLA (Fig. 11a).
 518 Conversely, the region to the east of 113.5°E along the section exhibited negative SLA anomalies. This
 519 weakening is consistent with the previous observations of the intensified warm core and decreased eddy
 520 area.



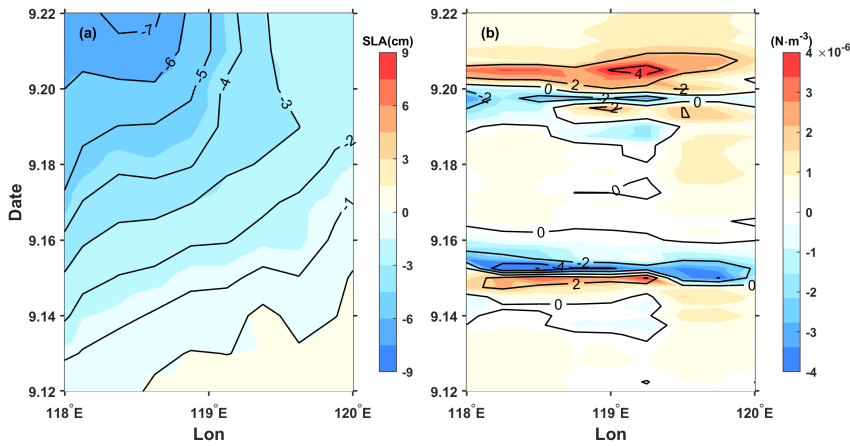
521
 522 **Figure 11.** The time/longitude plots of (a) SLA anomaly (cm) and (b) wind stress curl (N.m^{-3}) anomaly at the central
 523 section of AE1 (18.2°N). The anomalies were calculated relative to the average value of 10-13 September.

524 The response of AE2 differs from that of AE1 mainly because AE2 is quite near the Typhoon
 525 Kalmaegi's track. As the typhoon passes through AE2, the maximum wind radius is 48 km. AE2 is
 526 merely 26 km away from the typhoon center, essentially falling within two-times the maximum wind
 527 radius of the typhoon (Fig. 3). The significantly positive wind stress curl at the typhoon center induces
 528 upwelling and positive vorticity downward into the eddy (Huang and Wang, 2022), noticeably weakens
 529 the eddy, corresponding to the decrease in SLA (Fig. 12a). Furthermore, bases on the meridional
 530 isotherm profiles of the eddy center at three periods, it can be observed that during the passage of
 531 Typhoon Kalmaegi (15 September), the isotherms in the AE1 region exhibit significant subsidence (Fig.

删除了: After traversing the warm ocean characteristics of AE2, Typhoon Kalmaegi becomes stronger and the maximum wind radius becomes smaller. As it passes through AE1, the maximum wind radius is measured at 35 km. Notably, the center of AE1 is located outside the maximum wind radius, approximately 104 km away from the typhoon center (Fig. 3). Hence, the hypothesis presents here suggests that the observed intensification of AE1 on the left side of the typhoon track is more likely attributed to the negative wind stress generates outside the maximum wind radius, driving the enhancement of downwelling in the pre-existing anticyclonic feature in the ocean.

删除了: The response of AE2 is different from AE1 mainly because AE2 is quite near the typhoon Kalmaegi's track. When the typhoon passes through AE2, the maximum wind radius is 48km. AE2 is only 26 km away from the center of the typhoon, and its central area is basically within the maximum wind radius of the typhoon (Fig. 3). The significantly positive wind stress curl at the center of the typhoon induces upwelling and positive vorticity downward into the eddy (Huang and Wang, 2022), noticeably weakens the eddy, corresponding to the decrease in SLA (Fig. 12a)

552 13a), while in the AE2 region, the isotherms show uplift (Fig. 13b). This result aligns with the earlier
 553 observation that the convergence and subsidence within the warm eddy AE1 are enhanced by the
 554 influence of the wind stress curl induced by the typhoon, while the intensity of AE2 is weakened.



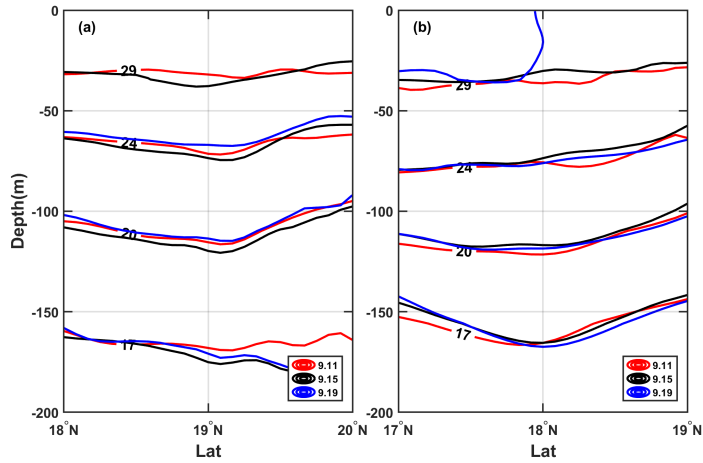
555
 556 **Figure 12.** Same as Fig.10, but for AE2(17.9 °N).

557 From the above, the relative position of eddies and the typhoon can influence the response of the
 558 eddies (Lu et al., 2020). The warm eddy AE1, located on the left side of the typhoon track, is not
 559 weakened by the strong cold suction effect caused by the typhoon Kalmaegi. Instead, it is strengthened
 560 due to the stronger negative wind stress curl generated by the typhoon.

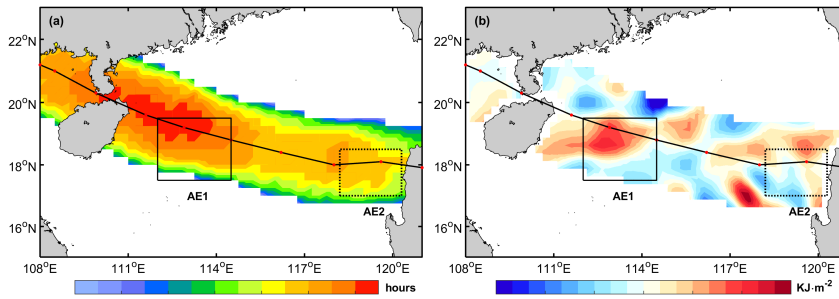
561 To understand the work done by the Typhoon Kalmaegi on the eddies in the ocean, we estimate the
 562 total work inputted into the ocean current u_c using the previously calculated wind stress (Liu et al.,
 563 2017):

564
$$W = \int \tau \cdot u_c dt . \quad (10)$$

565 Here, we select the region near the typhoon track where the wind speed exceeds $17 \text{ m}\cdot\text{s}^{-1}$ as the typhoon
 566 forcing region to understand the energy input by the typhoon to the warm eddy (Sun et al., 2010). The
 567 forcing duration over the ocean in the typhoon-affected region and the work done by the typhoon on the
 568 surface current are shown in Fig. 13. When the angle between the wind and the ocean current is acute,
 569 the typhoon does positive work on the ocean current. Conversely, when the angle is obtuse, the typhoon
 570 does negative work on the ocean current. It is evident that the region with the maximum forcing duration
 571 by the typhoon on AE1 corresponds to the area where the typhoon clearly does positive work on the
 572 ocean current, accumulating a work done exceeding 8 KJ m^{-2} . This acceleration of the flow velocity in
 573 the eddy results in convergence within the eddy and an increase in SLA, leading to the strengthening of
 574 AE1. On the other hand, the forcing duration by the typhoon on AE2 is smaller, and the typhoon does
 575 negative work on the ocean current in most areas, with a cumulative work done within -5 KJ m^{-2} , causing
 576 the flow velocity within the AE2 to decelerate.



577
 578 **Figure 13.** The meridional isotherm profiles of AE1 (a) and AE2 (b) before (11 September), during (15 September)
 579 and after (19 September) typhoon Kalmaegi.



581
 582 **Figure 14.** (a): the forcing time (unit: hours) of the typhoon; (b): the input work (unit: KJ. m⁻²) of the typhoon to
 583 the current.

584 **5. Summary**

585 Based on multi-satellite observations, on-site measurements, and numerical model data, we have
 586 gained valuable insights into the response of warm eddies AE1 and AE2 in the northern South China Sea
 587 to Typhoon Kalmaegi. Both horizontally and vertically, these eddies display distinct differences.
 588 Horizontally, we observe a reduction of areas by approximately 31% (AE1) and 36% (AE2). AE1,
 589 positions on the left side of the typhoon's track, strengthens with amplitude, R_o and EKE increasing by
 590 1.3 cm, 1.4×10^{-2} and $107.2 \text{ cm}^2 \cdot \text{s}^{-2}$ after the typhoon passed. In contrast, AE2, which intersects with the
 591 typhoon's track, weakens with amplitude, R_o and EKE decreasing by 3.1 cm, 1.6×10^{-2} and $38.5 \text{ cm}^2 \cdot \text{s}^{-2}$,
 592 respectively. Vertically, during the typhoon's passage, AE1 experiences intensified converging
 593 subsidence flow at its center, leading to an increase in temperature and a decrease in salinity above 150
 594 m. This response is more pronounced below the MLD (1.3°C) and persists for about a week after the

删除了: cm^2
 删除了: cm^2

597 typhoon. On the other hand, AE2 exhibits cooling above the MLD, accompanied by a decrease in salinity,
598 as well as a subsurface temperature drop and salinity increase due to the upwelling of cold water caused
599 by the typhoon's suction effect. The subsurface cooling and salinity increase in AE2 are further
600 influenced by Typhoon Fung-wong. Additionally, from the temperature vertical profile of Argo and in-
601 situ arrays, on 19 September, it can be seen that the non-eddy region also experiences significant cooling,
602 with a prominent cooling center observed at a depth of 60 m (-1.2 °C). The warm eddy AE2, influenced
603 by its own downwelling, exhibits enhanced mixing effects, resulting in a subsurface warm anomaly of
604 1.2 °C.

605 Further analysis reveals that the different responses of the warm eddies can be attributed to factors
606 such as wind stress curl distribution, which are influenced by the relative position of the warm eddies
607 and the typhoon track. The wind stress curl induced by the typhoon plays a crucial role in shaping the
608 response of the warm eddies. AE1, located on the left side of the typhoon's path, experiences prolonged
609 forcing from the typhoon, resulting in positive work on the ocean current. This inputs a strong negative
610 wind stress curl into the eddy, enhancing negative EPV and deepening D_E , so the downwelling within
611 the AE1 is obvious and contributing to its increased strength. In contrast, AE2, positioned directly below
612 the typhoon's track, experiences shorter forcing duration and weakens due to the strong positive wind
613 stress curl at the typhoon's center and shallower D_E . Furthermore, the absolute value of EPV increases in
614 both warm eddies during the typhoon's passage, but with differing impacts. The positive EPV contributes
615 to surface water cooling and the influx of cooler subsurface water, while the negative EPV facilitates
616 downwelling and intensifies the influence of the warm eddies.

617 **While numerous prior studies exploring the interaction between TCs and eddies have predominantly**
618 **drawn generalized conclusions, such as the weakening (strengthening) effect of cold (warm) eddies.**
619 **Conversely, TCs are recognized for strengthening cold eddies and weakening warm eddies. However,**
620 **our study takes a different approach. We aim to illustrate that even when TCs encounter eddies of the**
621 **same polarity, the response of these eddies to TCs exhibits variations. This nuanced response is intricately**
622 **linked to factors including the relative position of the eddies and the TCs, the eddies' intensity, and the**
623 **background current. It is discussed first time in the South China Sea. By analyzing wind stress curl**
624 **distribution, EPV, buoyancy frequency and the relative position between the eddies and the typhoon's**
625 **track, this case study provides a more nuanced understanding of the mechanisms driving these different**
626 **eddy-typhoon interactions in the Northern South China Sea. Moreover, it will further improve the**
627 **accuracy of TC forecasts and enhancing the simulation capabilities of air-sea coupled models.**

628
629
630 *Data availability.* The six-hourly best-track typhoon datasets were accessed on 3 February 2021 by JTWC,
631 <http://www.usno.navy.mil/JTWC>, JMA, [https://www.jma.go.jp/jma/jma-eng/jma-center/rsmc-hp-pub-](https://www.jma.go.jp/jma/jma-eng/jma-center/rsmc-hp-pub-eg/besttrack.html)
632 [eg/besttrack.html](http://tcdata.typhoon.gov.cn) and CMA, <http://tcdata.typhoon.gov.cn>. The AVISO product was accessed on 14 February
633 2021 by <https://marine.copernicus.eu/>. The AVHRR SST data was accessed on 16 March, 2022 by
634 ftp://podaac.jpl.nasa.gov/documents/dataset_docs/avhrr_pathfinder_sst.html. The Argo data was accessed
635 on 4 April, 2022 by <https://dataselection.euro-argo.eu/>. The wind data was accessed on 5 January, 2023 by

设置了格式: 突出显示

带格式的: 缩进: 首行缩进: 1 字符

删除了: In summary, the different responses of warm eddies to typhoons provide valuable insights into the complex interactions between the atmosphere and the ocean. Understanding these responses is crucial for accurate climate modeling and weather forecast. By investigating factors such as wind stress curl distribution, EPV, buoyancy frequency and the relative position of the eddies to the typhoon's track, researchers can gain a more precise understanding of the underlying mechanisms driving these interactions. This knowledge contributes to improved predictions and mitigation strategies for the impacts of typhoons and other extreme weather events, enhances the accuracy of climate models, and advances weather forecasting capabilities.

648 <https://apps.ecmwf.int/datasets/data/interim-full-daily/levtype=sfc/>. The GLORYS12V1 was accessed on
649 23 March, 2022 by <https://marine.copernicus.eu/>.

650 *Author contributions.* XYL and HZ contributed to the study conception and design. Material preparation, data
651 collection and analysis were performed by YHH and XYL. GQH and YL contributed to the methodology. The
652 original manuscript was prepared by XYL and YHH. All the authors contributed to the review and editing of
653 the manuscript.

654 *Competing interests.* The contact author has declared that none of the authors has any competing interests.

655 *Disclaimer.* Publisher's note: Copernicus Publications remains neutral with regard to jurisdictional claims in
656 published maps and institutional affiliations.

657 *Acknowledgements.* These data were collected and made freely available by JTWC, JMA, CMA, AVISO, AVHRR,
658 Argo, ECMWF, COPERNICUS. All figures were created using MATLAB, in particular using the M_Map toolbox
659 (Pawlowicz, 2020). The authors thank the anonymous reviewers, whose feedback led to substantial im-
660 provement of the resulting analyses, figures and manuscript

661 *Financial support.* This research has been supported by the National Natural Science Foundation of China
662 (42227901), Southern Marine Science and Engineering Guangdong Laboratory (Zhuhai), grant number
663 SML2020SP007 and SML2021SP207; the Innovation Group Project of Southern Marine Science and
664 Engineering Guangdong Laboratory (Zhuhai), grant number 311020004 and 311022001; the National
665 Natural Science Foundation of China, grant number 42206005; the open fund of State Key Laboratory of
666 Satellite Ocean Environment Dynamics, Second Institute of Oceanography, MNR, grant number QNHX2309;
667 General scientific research project of Zhejiang Provincial Department of Education, grant number
668 Y202250609; the Open Foundation from Marine Sciences in the First-Class Subjects of Zhejiang, grant number
669 OFMS006; State Key Laboratory of Tropical Oceanography (South China Sea Institute of Oceanology Chinese
670 Academy of Sciences), grant number LTO2220.

671

672

673

674 **References**

675 Cabanes, C., Grouazel, A., von Schuckmann, K., Hamon, M., Turpin, V., Coatanoan, C., Guinehut, S.,
676 Boone, C., Ferry, N., and Reverdin, G.: The CORA dataset: validation and diagnostics of ocean
677 temperature and salinity in situ measurements, *Ocean Sci. Discuss.*, 9, 1273-1312, 2012.

678 Chen, G., Hou, Y., and Chu, X.: Mesoscale eddies in the South China Sea: Mean properties,
679 spatiotemporal variability, and impact on thermohaline structure, *J. Geophys. Res.: Oceans*,
680 116, <https://doi.org/10.1029/2010jc006716>, 2011.

681 Chen Z, Yu F, Chen Z, et al. Downward Propagation and Trapping of Near-Inertial Waves by a
682 Westward-moving Anticyclonic Eddy in the Subtropical Northwestern Pacific Ocean[J]. *Journal of*
683 *Physical Oceanography*, 2023.

684 de Boyer Montégut, C.: Mixed layer depth over the global ocean: An examination of profile data and a
685 profile-based climatology, *J. Geophys. Res.: Oceans*, 109,<https://doi.org/10.1029/2004jc002378>, 2004.

686 Ezraty, R., Girard-Ardhuin, F., Piollé, J.-F., Kaleschke, L., and Heygster, G.: Arctic and Antarctic sea
687 ice concentration and Arctic sea ice drift estimated from Special Sensor Microwave data, *Département*
688 *d’Océanographie Physique et Spatiale, IFREMER, Brest, France and University of Bremen Germany*, 2,
689 2007.

690 Huang, L., Cao, R., and Zhang, S.: Distribution and Oceanic Dynamic Mechism of Precipitation Induced
691 by Typhoon Lekima, *American Journal of Climate Change*, 11, 133-
692 154,<https://doi.org/10.4236/ajcc.2022.112007>, 2022.

693 Huang, X. and Wang, G.: Response of a Mesoscale Dipole Eddy to the Passage of a Tropical Cyclone:
694 A Case Study Using Satellite Observations and Numerical Modeling, *Remote Sens.*,
695 14,<https://doi.org/10.3390/rs14122865>, 2022.

696 Jaimes, B. and Shay, L. K.: Enhanced Wind-Driven Downwelling Flow in Warm Oceanic Eddy Features
697 during the Intensification of Tropical Cyclone Isaac (2012): Observations and Theory, *J. Phys. Oceanogr.*,
698 45, 1667-1689,<https://doi.org/10.1175/jpo-d-14-0176.1>, 2015.

699 Jullien, S., Menkès, C. E., Marchesiello, P., Jourdain, N. C., Lengaigne, M., Koch-Larrouy, A., Lefèvre,
700 J., Vincent, E. M., and Faure, V.: Impact of tropical cyclones on the heat budget of the South Pacific
701 Ocean, *J. Phys. Oceanogr.*, 42, 1882-1906,<https://doi.org/10.1175/JPO-D-11-0133.1>, 2012.

702 Kessler, W. S.: The circulation of the eastern tropical Pacific: A review, *Prog. Oceanogr.*, 69, 181-
703 217,<https://doi.org/10.1016/j.pocan.2006.03.009>, 2006.

704 Li, Q., Sun, L., Liu, S., Xian, T., and Yan, Y.: A new mononuclear eddy identification method with
705 simple splitting strategies, *Remote Sens. Lett.*, 5, 65 - 72,<https://doi.org/10.1080/2150704x.2013.872814>,
706 2014.

707 Li, X., Zhang, X., Fu, D., and Liao, S.: Strengthening effect of super typhoon Rammasun (2014) on
708 upwelling and cold eddies in the South China Sea, *J. Oceanol. Limnol.*, 39, 403-
709 419,<https://doi.org/10.1007/s00343-020-9239-x>, 2021.

710 Lin, I. I., Chou, M.-D., and Wu, C.-C.: The Impact of a Warm Ocean Eddy on Typhoon Morakot (2009):
711 A Preliminary Study from Satellite Observations and Numerical Modelling, *TAO: Terrestrial,*
712 *Atmospheric and Oceanic Sciences*, 22,[https://doi.org/10.3319/tao.2011.08.19.01\(tm\)](https://doi.org/10.3319/tao.2011.08.19.01(tm)), 2011.

713 Lin, I. I., Wu, C.-C., Emanuel, K. A., Lee, I. H., Wu, C.-R., and Pun, I.-F.: The Interaction of
714 Supertyphoon Maemi (2003) with a Warm Ocean Eddy, *Mon. Weather Rev.*, 133, 2635-
715 2649,<https://doi.org/10.1175/MWR3005.1>, 2005.

716 Liu, F. and Tang, S.: Influence of the Interaction Between Typhoons and Oceanic Mesoscale Eddies on
717 Phytoplankton Blooms, *J. Geophys. Res.: Oceans*, 123, 2785-
718 2794,<https://doi.org/10.1029/2017jc013225>, 2018.

719 Liu, S.-S., Sun, L., Wu, Q., and Yang, Y.-J.: The responses of cyclonic and anticyclonic eddies to
720 typhoon forcing: The vertical temperature-salinity structure changes associated with the horizontal
721 convergence/divergence, *J. Geophys. Res.: Oceans*, 122, 4974-
722 4989,<https://doi.org/10.1002/2017JC012814>, 2017.

723 Lu, Z., Wang, G., and Shang, X.: Response of a Preexisting Cyclonic Ocean Eddy to a Typhoon, *J. Phys.*
724 *Oceanogr.*, 46, 2403-2410,<https://doi.org/10.1175/jpo-d-16-0040.1>, 2016.

725 Lu, Z., Wang, G., and Shang, X.: Strength and Spatial Structure of the Perturbation Induced by a Tropical
726 Cyclone to the Underlying Eddies, *J. Geophys. Res.: Oceans*, 125, <https://doi.org/10.1029/2020jc016097>,
727 2020.

728 Lu, Z., Wang, G., and Shang, X.: Observable large-scale impacts of tropical cyclones on subtropical gyre,
729 *J. Phys. Oceanogr.*, <https://doi.org/10.1175/JPO-D-22-0230.1>, 2023.

730 Ma, Z., Zhang, Z., Fei, J., and Wang, H.: Imprints of Tropical Cyclones on Structural Characteristics of
731 Mesoscale Oceanic Eddies Over the Western North Pacific, *Geophys. Res. Lett.*,
732 48, <https://doi.org/10.1029/2021gl092601>, 2021.

733 Ma, Z., Fei, J., Liu, L., Huang, X., and Li, Y.: An Investigation of the Influences of Mesoscale Ocean
734 Eddies on Tropical Cyclone Intensities, *Mon. Weather Rev.*, 145, 1181-
735 1201, <https://doi.org/10.1175/mwr-d-16-0253.1>, 2017.

736 Ning, J., Xu, Q., Zhang, H., Wang, T., and Fan, K.: Impact of Cyclonic Ocean Eddies on Upper Ocean
737 Thermodynamic Response to Typhoon Soudelor, *Remote Sens.*, 11, <https://doi.org/10.3390/rs11080938>,
738 2019.

739 Oey, L. Y., Ezer, T., Wang, D. P., Fan, S. J., and Yin, X. Q.: Loop Current warming by Hurricane Wilma,
740 *Geophys. Res. Lett.*, 33, <https://doi.org/10.1029/2006gl025873>, 2006.

741 Price, J. F.: Upper Ocean Response to a Hurricane, *J. Phys. Oceanogr.*, [https://doi.org/10.1175/1520-0485\(1981\)011%3C0153:UORTAH%3E2.0.CO;2](https://doi.org/10.1175/1520-0485(1981)011%3C0153:UORTAH%3E2.0.CO;2), 1981.

743 Pujol, M.-I., Faugère, Y., Taburet, G., Dupuy, S., Pelloquin, C., Ablain, M., and Picot, N.: DUACS
744 DT2014: the new multi-mission altimeter data set reprocessed over 20 years, *Ocean Sci.*, 12, 1067-
745 1090, <https://doi.org/10.5194/os-12-1067-2016>, 2016.

746 Rudzin, J. E. and Chen, S.: On the dynamics of the eradication of a warm core mesoscale eddy after the
747 passage of Hurricane Irma (2017), *Dyn. Atmos. Oceans*,
748 100, <https://doi.org/10.1016/j.dynatmoce.2022.101334>, 2022.

749 Shang, X.-d., Zhu, H.-b., Chen, G.-y., Xu, C., and Yang, Q.: Research on Cold Core Eddy Change and
750 Phytoplankton Bloom Induced by Typhoons: Case Studies in the South China Sea, *Adv. Meteorol.*, 2015,
751 1-19, <https://doi.org/10.1155/2015/340432>, 2015.

752 Shay, L. K. and Jaimes, B.: Mixed Layer Cooling in Mesoscale Oceanic Eddies during Hurricanes
753 Katrina and Rita, *Mon. Weather Rev.*, 137, 4188-4207, <https://doi.org/10.1175/2009mwr2849.1>, 2009.

754 Shay, L. K. and Jaimes, B.: Near-Inertial Wave Wake of Hurricanes Katrina and Rita over Mesoscale
755 Oceanic Eddies, *J. Phys. Oceanogr.*, 40, 1320-1337, <https://doi.org/10.1175/2010jpo4309.1>, 2010.

756 Shay, L. K., Goni, G. J., and Black, P. G.: Effects of a Warm Oceanic Feature on Hurricane Opal, *Mon.*
757 *Weather Rev.*, 128, 1366-1383, [https://doi.org/10.1175/1520-0493\(2000\)128<1366:EOAWOF>2.0.CO;2](https://doi.org/10.1175/1520-0493(2000)128<1366:EOAWOF>2.0.CO;2), 2000.

759 Song, D., Guo, L., Duan, Z., and Xiang, L.: Impact of Major Typhoons in 2016 on Sea Surface Features
760 in the Northwestern Pacific, *Water*, 10, <https://doi.org/10.3390/w10101326>, 2018.

761 Sun, J., Ju, X., Zheng, Q., Wang, G., Li, L., and Xiong, X.: Numerical Study of the Response of Typhoon
762 Hato (2017) to Grouped Mesoscale Eddies in the Northern South China Sea, *J. Geophys. Res.: Atmos.*,
763 128, <https://doi.org/10.1029/2022jd037266>, 2023.

764 Sun, L., Yang, Y., Xian, T., Lu, Z., and Fu, Y.: Strong enhancement of chlorophyll a concentration by a
765 weak typhoon, *Mar. Ecol. Prog. Ser.*, 404, 39-50, <https://doi.org/10.3354/meps08477>, 2010.

766 Sun, L., Li, Y.-X., Yang, Y.-J., Wu, Q., Chen, X.-T., Li, Q.-Y., Li, Y.-B., and Xian, T.: Effects of super
767 typhoons on cyclonic ocean eddies in the western North Pacific: A satellite data-based evaluation

768 between 2000 and 2008, *J. Geophys. Res.: Oceans*, 119, 5585-
769 5598,<https://doi.org/10.1002/2013jc009575>, 2014.

770 Thompson, B. and Tkalich, P.: Mixed layer thermodynamics of the Southern South China Sea, *Clim.*
771 *Dyn.*, 43, 2061-2075,<https://doi.org/10.1007/s00382-013-2030-3>, 2014.

772 Wada, A. and Usui, N.: Impacts of Oceanic Preexisting Conditions on Predictions of Typhoon Hai-Tang
773 in 2005, *Adv. Meteorol.*, 2010, 756071,<https://doi.org/10.1155/2010/756071>, 2010.

774 Walker, N. D., Leben, R. R., and Balasubramanian, S.: Hurricane-forced upwelling and
775 chlorophyllaenhancement within cold-core cyclones in the Gulf of Mexico, *Geophys. Res. Lett.*, 32, n/a-
776 n/a,<https://doi.org/10.1029/2005gl023716>, 2005.

777 Wang, G., Su, J., Ding, Y., and Chen, D.: Tropical cyclone genesis over the south China sea, *J. Mar.*
778 *Syst.*, 68, 318-326,<https://doi.org/10.1016/j.jmarsys.2006.12.002>, 2007.

779 Wang, G., Zhao, B., Qiao, F., and Zhao, C.: Rapid intensification of Super Typhoon Haiyan: the
780 important role of a warm-core ocean eddy, *Ocean Dyn.*, 68, 1649-1661,[https://doi.org/10.1007/s10236-](https://doi.org/10.1007/s10236-018-1217-x)
781 [018-1217-x](https://doi.org/10.1007/s10236-018-1217-x), 2018.

782 Xiu, P., Chai, F., Shi, L., Xue, H., and Chao, Y.: A census of eddy activities in the South China Sea
783 during 1993–2007, *J. Geophys. Res.: Oceans*, 115,<https://doi.org/10.1029/2009jc005657>, 2010.

784 Yan, Y., Li, L., and Wang, C.: The effects of oceanic barrier layer on the upper ocean response to tropical
785 cyclones, *J. Geophys. Res.: Oceans*, 122, 4829-4844,<https://doi.org/10.1002/2017jc012694>, 2017.

786 Yu, F., Yang, Q., Chen, G., and Li, Q.: The response of cyclonic eddies to typhoons based on satellite
787 remote sensing data for 2001–2014 from the South China Sea, *Oceanologia*, 61, 265-
788 275,<https://doi.org/10.1016/j.oceano.2018.11.005>, 2019.

789 Yu, J., Lin, S., Jiang, Y., and Wang, Y.: Modulation of Typhoon-Induced Sea Surface Cooling by
790 Preexisting Eddies in the South China Sea, *Water*, 13,<https://doi.org/10.3390/w13050653>, 2021.

791 Zhang, H.: Modulation of Upper Ocean Vertical Temperature Structure and Heat Content by a Fast-
792 Moving Tropical Cyclone, *J. Phys. Oceanogr.*, 53, 493-508,<https://doi.org/10.1175/jpo-d-22-0132.1>,
793 2022.

794 Zhang, H., Chen, D., Zhou, L., Liu, X., Ding, T., and Zhou, B.: Upper ocean response to typhoon
795 Kalmaegi (2014), *J. Geophys. Res.: Oceans*, 121, 6520-6535,<https://doi.org/10.1002/2016jc012064>,
796 2016.

797 Zhang, Y., Zhang, Z., Chen, D., Qiu, B., and Wang, W.: Strengthening of the Kuroshio current by
798 intensifying tropical cyclones, *Science*, 368, 988-993,<https://doi.org/10.1126/science.aax5758>, 2020.

799